ALLPRESS, J. G. & SANDERS, J. V. (1972). In *Electron Microscopy and structure of Materials*. Edited by G. THOMAS, p. 134. Berkeley, California: Univ. of California Press. (To be published).

ALLPRESS, J. G., SANDERS, J. V. & WADSLEY, A. D. (1969). *Acta Cryst.* B25, 1156.

ALLPRESS, J. G. & WADSLEY, A. D. (1969). *J. Solid State Chem.* 1, 28.

ANDERSSON, S., MUMME, W. G. & WADSLEY, A. D. (1966). *Acta Cryst.* 21, 802.

CHIDZEY, E. A. (1970). M. Sc. Thesis, University of Melbourne.

COCKAYNE, D. J. H., PARSONS, J. R. & HOELKE, C. W. (1971). *Phil. Mag.* 24, 139.

COWLEY, J. M. (1967). In *Progress in Materials Science*. vol. 13, No. 6, p. 267, Edited by B. CHALMERS and W. HUME-ROTHERY. Oxford: Pergamon Press.

COWLEY, J. M. & IIJIMA, S. (1972). *Z. Naturforsch.* 27a, 445.

COWLEY, J. M. & MOODIE, A. F. (1957). *Acta Cryst.* 10, 609.

COWLEY, J. M. & MOODIE, A. F. (1960). *Proc. Phys. Soc.* 76, 378.

COWLEY, J. M. & MOODIE, A. F. (1962). *J. Phys. Soc. Japan*, 17, Suppl. BII, p. 86.

DOWELL, W. C. T. (1963). *Optik*, 20, 535

DOWELL, W. C. T., FARRANT, J. L. & McLEAN, J. D. 1968. In *Proceedings of the Fourth European Regional Conference on Electron Microscopy, Rome*, p. 583.

GOODMAN, P. & MOODIE, A. F. (1972). Submitted to *Acta Cryst.*

HASHIMOTO, H., MANNAMI, M. & NAIKI, T. (1961). *Phil. Trans.* A253, 459.

HEAD, A. K. (1967). *Aust. J. Phys.* 20, 557.

IIJIMA, S. (1971). *J. Appl. Phys.* 42, 5891.

LYNCH, D. F. (1971). *Acta Cryst.* A27, 399.

LYNCH, D. F. & O'KEEFE, M. A. (1972). *Acta Cryst.* A28, 536.

MOODIE, A. F. (1972a). *Z. Naturforsch.* 27a, 437.

MOODIE, A. F. (1972b). Submitted to *Phil. Mag.*

MIYAKE, S., FUJIWARA, K., TOKONAMI, M. & FUJIMOTO, F. (1964). *Jap. J. Appl. Phys.* 3, 276.

ROTH, R. S. WADSLEY, A. D. (1964a). *Acta Cryst.* 19, 32.

ROTH, R. S. & WADSLEY, A. D. (1964b) *Acta Cryst.* 19, 38.

WADSLEY, A. D. (1955.) *Rev. Pure Appl. Chem.* 5, 165.

WADSLEY, A. D. & ANDERSSON, S. (1970). In *Perspectives in Structural Chemistry*, Vol. 3, p.l. Edited by J. D. DUNITZ & J. A. IBERS, New York: Wiley.

YADA, K. & HIBI, T. (1969). *J. Electron Microsc.* 18, 266.

ZERNIKE, F. (1942). *Physica*, 9, 686.

n-Beam Lattice Images.
II. Methods of Calculation

BY D. F. LYNCH

Division of Chemical Physics, CSIRO, P. O. Box 160, Clayton, Victoria, Australia, 3168

AND M. A. O'KEEFE

Division of Tribophysics, CSIRO, University of Melbourne, Victoria, Australia, 3052

The calculation of amplitudes and phases of beams of electrons diffracted from thin (≤ 100 nm) crystals of $W_4Nb_{26}O_{77}$ is described. These diffraction data are used to compute 11-beam 00*l* electron microscope lattice images and the effects of instrument aberrations are considered. Several approximations are compared with a more exact 435-beam, two-dimensional computation, and with experimental diffraction data and lattice images. Finally, the projected charge density approximation to image contrast is evaluated.

1. Introduction

In the first paper in this series (Allpress, Hewat, Moodie & Sanders, 1972) (referred to as I hereafter), an account of the theory of electron scattering and imaging is given. The agreement obtained between experimental and calculated images is shown to be quite good when applied to 11-beam, 00*l* images from the complex oxide $W_4Nb_{26}O_{77}$. In this paper, calculations which produce these results are described and ways given to incorporate instrumental effects in the calculation. The effects include:

(i) Spherical aberration

(ii) Chromatic aberration

(iii) Beam divergence.

Methods of calculation of electron scattering problems have been described elsewhere (Cowley & Moodie, 1957; Goodman & Moodie, 1972). These use both multislice and phase-grating methods to calculate

diffraction amplitudes and phases. The method of Cowley & Moodie (1960) can be used to calculate electron images using these amplitudes and phases. Methods of doing this were first developed in this laboratory by Hewat (1970). Previous calculations (Goodman & Lehmpfuhl, 1967; Johnson, 1968; Lynch, 1971) were carried out on substances having small unit cells with only a few atoms per unit cell. We have carried out calculations for the oxide $W_4Nb_{26}O_{77}$ which has a large unit cell containing 214 atoms and gives lattice fringes with periodicities of the order of 2·6 nm. Due to this large unit-cell size, it was necessary to re-evaluate the types of approximations which can be made in the n-beam scattering calculations, compared with those which had previously been made.

In this communication none of the calculations made has included effects of inelastic scattering. Such effects would be represented by means of phenomenological absorption parameters. However the term 'weak-beam absorption' is used in the restricted sense of low normalization of the calculated results occurring due to the inclusion of an insufficient number of dynamically coupled reflexions from the thin phase grating.

The most exact calculation which could be made was a two-dimensional multislice calculation involving coupling of sufficient reflexions in the zone of interest. This zone is defined as that whose axis is most nearly parallel to the illuminating beam. In the case of the oxide considered in these calculations, 435 reflexions gave adequate normalization.
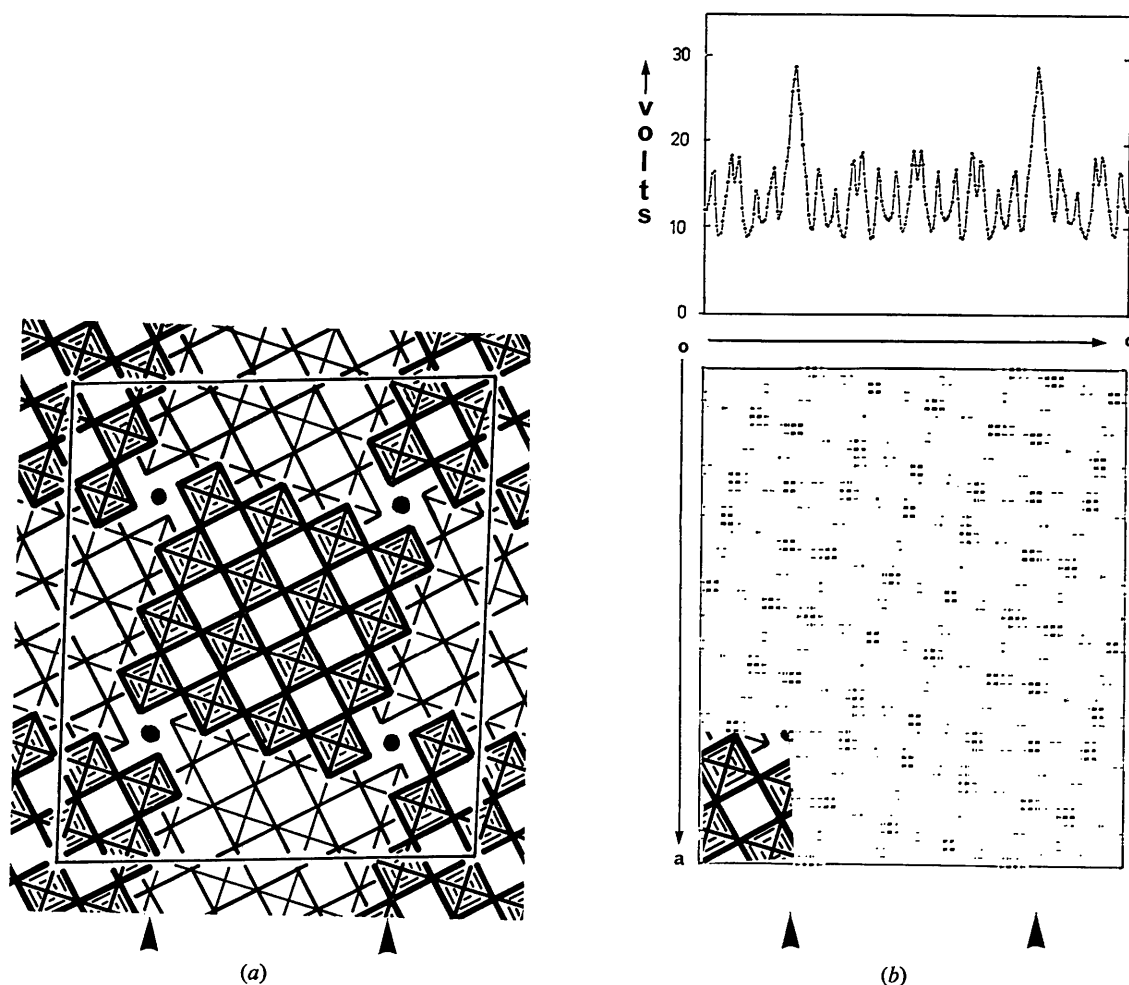

(a)

(b)

Fig. 1. (a) Idealized model of the structure of $W_4Nb_{26}O_{77}$, viewed down [010]. Each square represents an octahedron, the lighter and darker squares being centred on parallel planes 0·19 nm apart. The octahedra form blocks of 4×3 and 4×4 by sharing corners, and these blocks are joined to one another by sharing octahedral edges, along the crystallographic shear planes (arrowed). The circles represent tungsten atoms in tetrahedral coordination. (b) Projected potentials of $W_4Nb_{26}O_{77}$. The half-tone picture is the projection of the structure down the b axis. The projected potential $\varphi_p(x, y)$ has been calculated on a 60×60 net. Any projected potential less than 20 V produces no contrast in the display. The darkest areas are those greater than 105 V. The upper graph is then the one-dimensional projection $\varphi_p(x)$ onto the c axis. The large peaks at approximately $\frac{1}{4}c$ and $\frac{3}{4}c$ are at the projected positions of the tungsten atoms occupying tetrahedral sites in the crystallographic shear planes.

The systematics approximation (Hoerni, 1956) that was used considers dynamical coupling along a systematics line of reflexions in the zone only. The systematics multislice (Goodman & Lehmpfuhl, 1967) was thus a one-dimensional approximation to the two-dimensional multislice. Two ways of obtaining a systematics approximation are to:-

(i) multislice from a one-dimensional phase grating; and

(ii) multislice with a systematics line from a two-dimensional phase grating.

The phase-grating approximation (Cowley & Moodie, 1960) is of interest in two ways. Firstly, to determine a suitable phase grating for use in the multislice operation, and secondly, to use a phase grating as an approximation to determine the electron amplitudes and phases.

A kinematic approximation was also tested. In this approximation, the central beam amplitude was set at unity and phase set at 0. The amplitudes of the scattered beams, phase set at $\pi/2$, were given by multiplication of the shape transform with scattering amplitude.

The validity of the charge-density approximation (Cowley & Moodie, 1960, and also I) was tested by calculating this directly for the crystal using the same number of Fourier coefficients as the number of beams allowed through the aperture to form an image in the lattice-image calculation.

These approximations were checked in two ways; (i) by comparison with the most accurate two-dimensional multislice and (ii) by comparison with experimental diffraction intensities and lattice images.

2. The object

The oxide considered was $W_4Nb_{26}O_{77}$. The structure has been determined by X-ray measurements (Andersson, Mumme & Wadsley, 1966). The unit cell constants are $a = 2\cdot974$ nm, $b = 0\cdot3824$ nm, $c = 2\cdot597$ nm, and $\beta = 1\cdot611$ rad, and the structure (as seen when viewed down the short b axis) is shown in Fig. 1(a).

Structure amplitudes were calculated from the published atom positions and from electron form-factor curves derived from published X-ray form factors (Cromer & Waber, 1965) using the Mott formula (Mott, 1930). The calculated structure amplitudes were summed to obtain the projected potential distributions across the unit cell. A projection parallel to the short b axis was used. These projected potential distributions were used as the starting point for the n-beam scattering calculations. Representations of the one-dimensional and two-dimensional projected potentials are shown in Fig. 1(b). Because the structure has 214 atoms in the unit cell, care must be taken to ensure that a sufficient number of structure factors are used in order to define the shapes of individual atoms. It was found that up to 120 orders were sufficient in the systematics

case, which corresponded to defining the systematics potential to 1/240th of the unit cell. In the two-dimensional case, 30 orders on both axes were taken, defining the potential on a 60×60 net.

In Fig. 2 is shown a flow sheet demonstrating the various procedures which may be used to calculate image profiles in an electron microscope. All of the indicated paths have been explored in the calculation of images presented in the report. There is no inherent difficulty in extending the present calculations to the calculation of two-dimensional lattice images. Except for the charge-density approximation all the procedures require a good estimation of the crystal structure in order to calculate the image. In the charge-density case the image can be used to determine the coarse structure of the object.
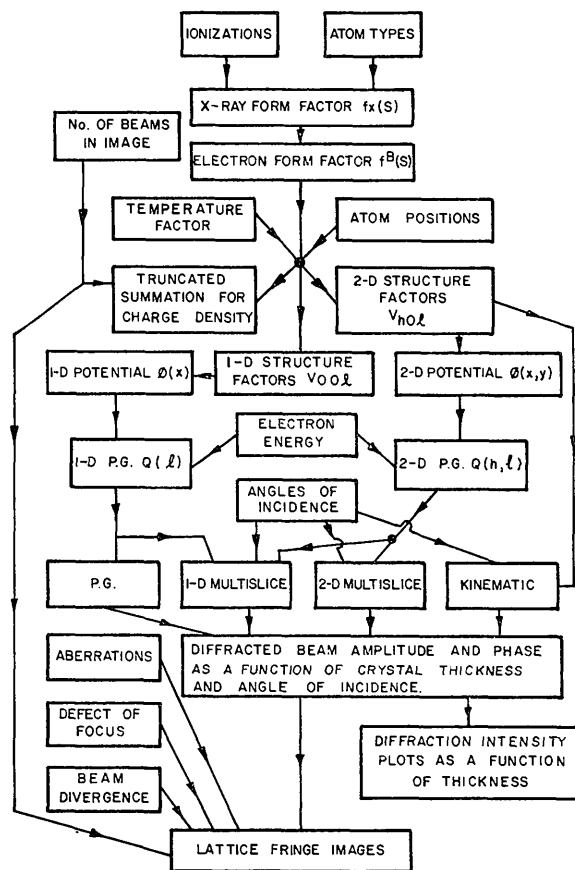

Fig. 2. A flow chart which illustrates the procedures that may be used to calculate lattice images. P. G. is the abbreviation for phase grating. The most time-consuming part of the calculation is the multislice operation. This is avoided in the projected charge density calculation, which evaluates a truncated projected charge density by a Fourier summation over only those beams which contribute to the formation of the image. The image approximates to this summation for certain ranges of crystal thickness and defect of focus. The effects of changes in angle of incidence on the P.G. results were not investigated as the angles involved were small ($<0\cdot1$ rad).
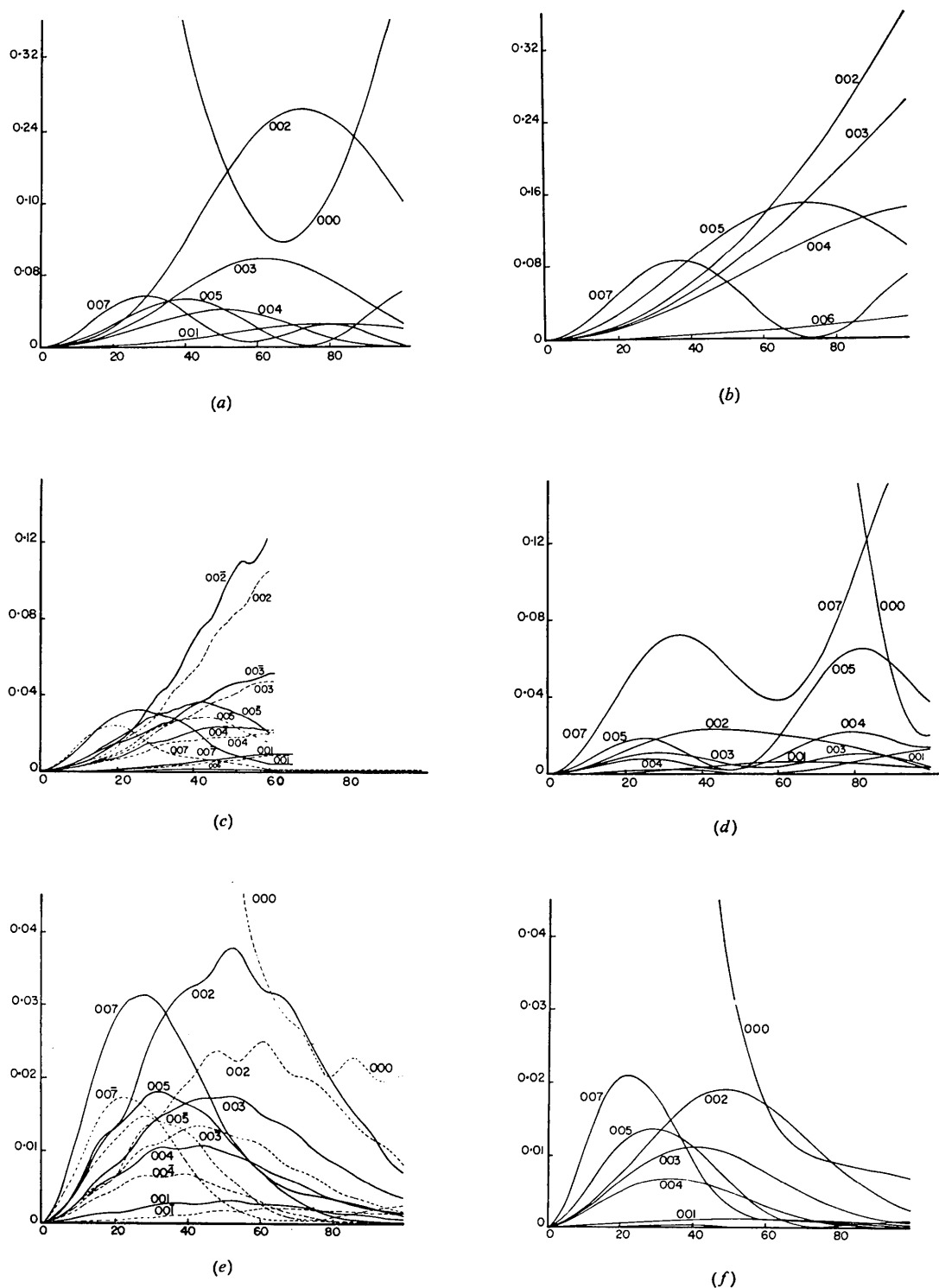
Fig. 3. Beam intensities as a function of crystal thickness for the 00*l* reflexions, *l* = 1 to 7. (*a*) Systematics calculation from a one-dimensional phase grating. (*b*) Kinematic calculation. The 001 is too weak, and the 000 too strong to appear on scale. (*c*) Two-dimensional multislice calculation (435 reflexions) computed to a 60 nm thickness only. The 000 reflexion is too intense to appear on scale. (*d*) One-dimensional thick-phase-grating calculation. (*e*) Two-dimensional multislice calculation (105 reflexions). Note the change in vertical scale made necessary by the heavy weak-beam absorption. (*f*) Systematic calculation from a two-dimensional phase grating. Note that again there has been heavy weak-beam absorption. In (*a*), (*d*), (*e*) and (*f*) the 006 is too weak to appear on scale.

3. Scattering calculations

3.1 *The thin phase grating*

The first step in calculation of dynamic phases and amplitudes by multislice methods is to calculate the thin phase grating which is the transmission function for a thin slice of the crystal.

The thin phase grating is defined as:

$$q(x,y) = \exp\{i\sigma\varphi_p(x,y) \cdot \Delta z\},$$

where $\sigma = \dfrac{\pi}{\lambda W} \cdot \dfrac{2}{1+(1-\beta^2)^{1/2}}$, λ is the relativistic elec-

tron wave length, W is the acceleration potential in volts, $\varphi_p(x,y)$ is the projected potential, and Δz is the slice thickness. It is then usual to deal with the Fourier transform of q,

$$Q(h,l) = \int_0^a \int_0^b q(x,y) \exp\left\{2\pi i\left(h\frac{x}{a} + l\frac{y}{b}\right)\right\} dx\,dy.$$

The number of reflexions in the phase grating must be sufficiently great that the sum of intensities is as close as possible to the incident wave intensity. In the one-dimensional case, the phase grating was determined to the 14th order (29 reflexions) and in the two-dimensional case also to the 14th order (435 reflexions). In the one-dimensional case, normalization was very good at 0·99998 and in the two-dimensional case normalization was 0·9998. There are several conditions which are imposed on the choice of the magnitude of Δz. Because of the use of Fourier transformations, if Δz is so large that $\exp(i\sigma\varphi_p\Delta z)$ has more turning points than the original structure, the Fourier transformation requires many more sampling points. Secondly, Δz must be sufficiently small so that the propagation function used in the multislice calculation does not give pseudo-upper-layer-line reinforcement on any of the reflexions propagated. In this case Δz was limited to 0·5 nm in the one-dimensional case and 0·2 nm in the two-dimensional case. Thus, in both cases, quite satisfactory thin phase grating calculations could be made – adequate both as an input to one-dimensional and two-dimensional multislice calculations and for phase grating calculations.

3.2 *Multislice calculation*

Three types of multislice calculations were made (Fig. 2). These can be arranged in order of time of calculation as (i) systematics multislice and (ii) systematics from a two-dimensional phase grating, taking equal time, and (iii) full two-dimensional multislice calculation. The multislice operation is the most time-consuming part of the calculation, since the time of calculation is proportional to N^2, where N is the number of reflexions. The systematics approximation, which greatly reduces the number of beams to be multisliced, gives a large gain in calculation speed. The 435-beam multislice calculation took approxi-

mately half a minute per slice on a CDC 3600 computer.

The propagation function in the multislice operation defines the angle of incidence for that particular calculation. Calculations were carried out over the range of angles of incidence corresponding to the measured cone of convergence for a JEM 100B, *i.e.* a semi-angle of $6\cdot4 \times 10^{-4}$ rad. This cone was sampled at 11 points, the variation in diffracted wave amplitude and phase being sufficiently slow across this angle so that no finer sampling was needed.

The multislice calculation took the standard form which gives the scattered wave amplitudes and phases from the *n*th slice in terms of the $(n-1)$th slice output, modified by the propagation function:

$$U_n(h,k) = [U_{n-1}(h,k) \cdot P(h,k)] * Q(h,k)$$

where

* denotes convolution,

$Q(h,k)$ is the Fourier coefficient for a thin phase grating,

$U_n(h,k)$ is the wave amplitude and phase from the *n*th slice,

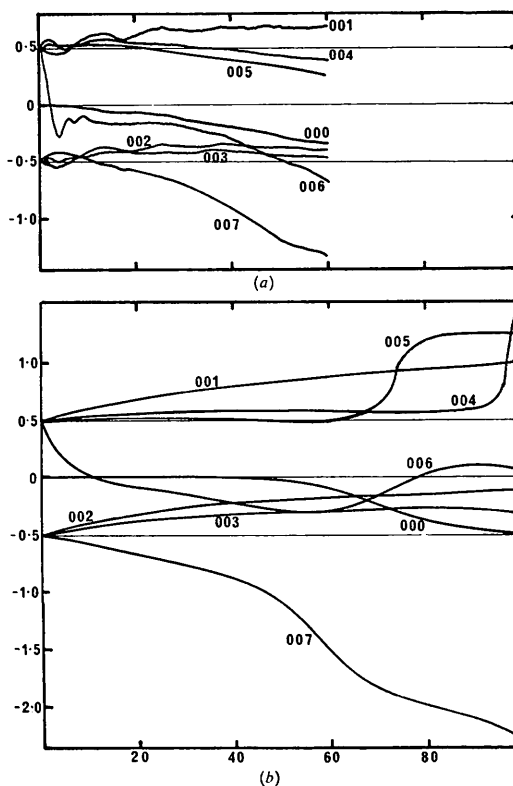Fig. 4. Phase of scattered beams as a function of crystal thickness. The vertical scale is in units of π, the horizontal lines at 0 and $\pm 0\cdot5\pi$ are the phase variation to be expected from a kinematic calculation. (*a*) Two-dimensional multislice calculation (435 reflexions). (*b*) Systematics calculation from a one-dimensional phase grating.

and

$P(h,k)$ is the propagation function.

$$P(h,k) = \exp\{2\pi i\zeta(h,k)\Delta z\},$$

where Δz is the slice thickness and $\zeta(h,k)$ is the excitation error for (h,k)th reflexion for a particular angle of incidence.

The number of beams in a multislice calculation must be such that the sum of intensities of beams at the final thickness should be very close to 1. In the one-dimensional case, 29 reflexions were sufficient to maintain a normalization of 0·96 at 100 nm and the two-dimensional case was only marginally satisfactory for 435 beams, the normalization being 0·72 at 60 nm.

A two-dimensional multislice calculation was also carried out for 105 reflexions. In this case, there was heavy weak-beam absorption such that, at a thickness of 30 nm, the normalization was 0·44, at 60 nm it was 0·17, and at 100 nm it was 0·05.

Because the short axis (0·3824 nm) of the crystal was normal to the plane of the slice, it was felt that upper layer line effects could be neglected in the most exact calculation. This short axis corresponds to an upper layer spacing of approximately 2·5 nm^{-1}. The largest excitation error in any of the arrays multisliced was $-0\cdot57$ nm^{-1}, which is only one quarter of the upper layer line spacing.

3.3 Phase grating

The scattered wave from a crystal of thickness H can be approximated by $\exp(i\sigma\varphi_p H)$, the phase grating. This approximation gives the correct dynamical coupling between diffracted beams but represents the Ewald sphere as a plane and thus gives too great a weight to outer reflexions. In practice, its calculation takes as long as the multislice calculation. It is possible, of course, to calculate the phase grating as if it were a thin phase grating with large Δz; however, this implies a very fine sampling interval, since $q(x,y)$ will be a rapidly oscillating function in the unit cell. Another method of calculating this approximation is to use the usual multislice recurrence relation with unit propagation, i.e. $U_n(h,k) = U_{n-1}(h,k) * Q(h,k)$, where $U_n(h,k)$ is the wave output of the nth slice and $Q(h,k)$ is the thin phase grating. In practice, this method takes as much calculation time as the multislice. Thus, the approximation is of interest only as a valid approximation of the scattering process, but it is not as exact as the multislice calculation.

3.4 Kinematic calculation

If the scattering from a finite parallel-sided slab of crystal is described by the first Born approximation, the central beam has unit intensity and all diffracted beams are equal to the respective Fourier coefficients of the projected potential multiplied by a phase factor of $\pi/2$ as well as a factor due to the shape transform of the crystal slab. To calculate the image, the scattered beams passing through the aperture are propa-

gated and Fourier summed in the usual way. For thickness H, the scattered wave may be written as

$$U(h,k) = iV(h,k) \cdot H \cdot \frac{\sin \pi\zeta(h,k) \cdot H}{\pi\zeta(h,k) \cdot H}$$

and

$$U(0,0) \cdot H = 1.$$

This approximation to imaging is that used by Zernicke (1942) in his description of the phase contrast method of imaging in the optical microscope. Thus, in the kinematic approximation, the central beam, $U(0,0)$, is constant for all thicknesses. The calculation time is extremely short because there is no convolution. It is a valid series approximation of the scattering function and, as it is a very fast calculation, it has been evaluated along with the other methods.

3.5 Charge density

In Paper I and Cowley & Moodie (1960), a very simple approximation to image contrast was given. This approximation stated that for a small defect of focus from a Fourier image plane the image contrast is given by

$$I(x,y) = qq^* \left[1 - \frac{\varepsilon\sigma\lambda}{2\pi} \cdot \nabla^2\varphi_p(x,y) \right]$$

and

$$\varrho_p(x,y) \propto \nabla^2\varphi_p(x,y),$$

where $q(x,y)$ is the wave transmitted through the objective aperture as calculated by a thick phase grating approximation, $\sigma = \dfrac{\pi}{\lambda W}$, λ is the wavelength of electron beam, $\varepsilon = $ defect of focus and $\varrho_p(x,y)$ is the projected total charge-density distribution in the unit cell, both electronic and nuclear. The approximation is made that $qq^* = 1$ for the aperture used and hence the image contrast becomes simply a matter of evaluating $\varrho_p(x,y)$.

From Poisson's equation it can be shown that

$$\varrho_p(x,y) \propto \nabla^2\varphi_p(x,y) = -16\pi^2 \cdot H$$
$$\times \sum_h \sum_k \exp\{2\pi i(hx + ky)\} \cdot V(h,k) \cdot S^2(h,k),$$

where $S(h,k) = \dfrac{\sin \theta(h,k)}{\lambda}$, H is crystal thickness, $\varrho_p(x,y)$ is the projected charge density, $V(h,k)$ is the structure amplitude, and $\theta(h,k)$ the Bragg angle for the (h,k)th reflexion. This is a simple calculation, and quite fast, and if it is sufficiently accurate it allows naive interpretation of the images in terms of the projected charge density of the structure.

Substitution of the expression for ϱ_p into the equation for image intensity shows that image intensity is linearly dependent on both defect of focus, ε, and crystal thickness, H. Thus images calculated by this approximation are displayed as a function of the product εH.
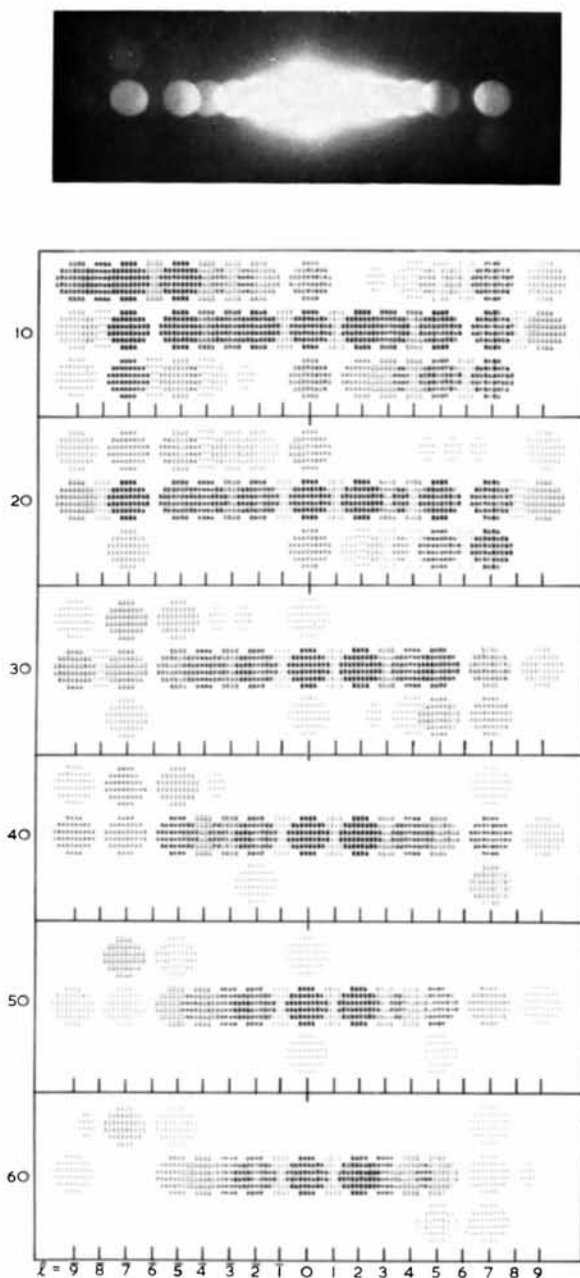
Fig. 5. Intensity of diffracted beams displayed by half-tone method for six crystal thicknesses for l ranging between -9 and $+9$ and h ranging from -2 to $+2$. For comparison a selected area diffraction pattern from a crystal approximately 30 nm thick is shown at the top of the figure. The calculation was made for an angle of incidence of 0·0996 rad from the zone axis while maintaining equal excitation of the 002 and 00$\bar{2}$ reflexions.

4. Imaging

Given the phases and amplitudes of the diffracted beams, the Fourier summation of these gives the intensity distribution for Gaussian focus. Inclusion of a propagation function of the standard form gives the image contrast for different defects of focus, each defect of focus being associated with a particular propagation value. Magnification is a simple multiplicative factor and for convenience is usually chosen to be 1. Since we are dealing with a periodic object, absolute scale is of no interest.

The propagation function for imaging is $P(h,k) =$ exp $\{2\pi i \cdot \zeta(h,k) \cdot \varepsilon\}$, where ε is the defect of focus in nm, defined as positive for overfocus, $\zeta(h,k)$ are excitation errors as defined in the multislice calculation and are, in fact, the means of defining the spherical wave front propagated from the focal plane.

4.1 Divergence

Small variations of angle of incidence at zero defect of focus do not change the form of the imaging calculation and any change in the image observed can only be due to variation of wave amplitude and phases as a function of angle of incidence. For non-zero defect of focus, the principal effect is a lateral displacement of the image, which is proportional to the magnitude of the defect of focus and to the angle. For large defects of focus, this dominates any effect due to variations with angle of the scattered wave amplitudes and phases. Hence, the major effect (at large defects of focus) of a cone of angles of incidence, is to smear out the detail of any images observed. This occurs for a defect of focus greater than 200 nm for $W_4Nb_{26}O_{77}$ and a semi-angle of $6\cdot4 \times 10^{-4}$ radian. In practice, for a real electron microscope, it is necessary to sum over angles of incidence corresponding to the cone of illumination at the specimen.

4.2 Aberration effects
Chromatic aberration

The spread in electron energies in the illuminating beam causes, at first order, chromatic aberration. As shown by Hewat (1970), the effect of this on an image may be taken into account by adding together images over a small range of defects of focus (± 10 nm in 2 nm steps). In practice, this would depend on the individual instrument's monochromation in the illumination system.

Spherical aberration

For a lens of known spherical aberration coefficient (Hewat, 1970), one may write in an effect of this spherical aberration on the propagation function for the aperture used and include this in the imaging program. The phase delay of a beam at angle α to the axis is $\frac{2\pi}{4\lambda} C_s\alpha^4$, where C_s is the spherical aberration coefficient of the lens.

This phase delay is incorporated into the propagation function and may be represented as an effective difference in defect of focus for each beam. The effect of spherical aberration is obviously heavily dependent on the size of aperture used in the calculation, *i.e.*, the size of α.

4.3 Image display

For display of calculated results of images, two methods were adopted. Firstly, graphs were plotted of intensity across the unit cell at a precision of 1/10th as a character graph printed by standard means on a line printer. Lateral definition was for 3 unit cells at 1/40th parts of a unit cell.

The second and most useful display is by means of a half-tone printing routine (Head, 1967) which allows a photographic representation which gives 10 shades of grey from white to dark grey for direct comparison with experimental images.

5. Results

5.1 Results from scattering calculations

At the first level, we have results of scattering calculations in the form of scattered amplitudes and phases as a function of crystal thickness and angle of incidence. The most useful way of intercomparison of methods was by means of displays showing intensity of various reflexions as a function of crystal thickness at a fixed angle of incidence. For direct comparison with selected area diffraction patterns, intensities of diffracted beams were displayed by the half-tone output in disc patterns arranged in approximately the same way as in a diffraction pattern. These patterns from the full two-dimensional multislice calculation were very useful for determining the approximate crystal thickness from selected area diffraction patterns. Also, beam phase was graphed as a function of crystal thickness for various reflexions. This gave a measurement of the degree to which the calculation was non-kinematic.

In Fig. 3(c) are shown curves from the two-dimensional multislice calculation. Although the orientation for these curves is the symmetric systematic orientation (*i.e.* 002 and 00$\bar{2}$ are equally excited), it can be seen that there is a marked difference in the curve for 002 and 00$\bar{2}$ due to the non-systematic interactions; the strong sublattice reflexions lie at a small angle to the reciprocal lattice basis axes. Of course, as shown in Fig. 3(a), (f), the systematic calculations, both from a two-dimensional phase grating and pure systematics, do not show this difference between symmetry-related pairs.

The phase grating curves [Fig. 3(d)] show that this approximation appears to break down at 20 nm compared with systematics calculation.

Some calculations were also made for a 105-beam array. As can be seen from Fig. 3(e), the absorption is quite high, due to the fact that the array is not large enough, with the result that the curves differ slightly

from those formed from the two-dimensional array of 435 reflexions.

The curves from the kinematic calculation as shown in Fig. 3(*b*) appear to give quite good agreement for thin crystals (approximately 5 nm). However, as can be seen in Fig. 4 the phases of the beams in the kinematic model are quite in error even for very thin crystals. Thus, it seems that the kinematic approximation is not satisfactory.

For comparison with experiment, the disc pattern outputs shown in Fig. 5 were quite effective especially in regard to their off-systematic reflexion intensities and the relative weights of 007, 005 and 002 reflexions. The first-order reflexion is always weak in all experimental patterns and this could be reproduced by theoretical calculation only if non-ionized form factors were used in the structure factor calculations (Anstis, Lynch, Moodie & O'Keefe, 1972). The systematic orientations are defined by the sets of angles of incidence which equally excited 002 and 00$\bar{2}$.

For the two-dimensional multislice calculations, the systematics orientation was obtained by tilting away from the zone axis while maintaining the equal excitation of 002, 00$\bar{2}$. Several angles ranging from 0·07 to 0·17 rad were tried to determine the effect of this change of tilt on the beam intensity *versus* crystal thickness plots. The range of angles was chosen on the basis of the diameter of the first Laue circle appearing in the experimental selected area diffraction pattern. No significant effect was observed.

5.2 *Results from image calculations*

In Fig. 6 are shown sets of calculated images for all the methods of calculation except the charge density approximation for a range of defects of focus at a fixed crystal thickness of 30 nm. Although other thicknesses could be chosen, this value was selected for comparison with experimental images from a crystal of that thickness. Similarly, to match the experiment, 11 beams were allowed through the aperture, although more or less could have been used.

On the basis that the images from the two-dimensional multislice are the most exact, the amount by which the other images deviate from these is a measure of the error incurred by the approximation for that crystal thickness. For this particular structure, it would appear that any approximation to the most exact calculation gave detectable differences in image contrast. However, the effects on these images of the instrumental parameters of chromatic aberration, spherical aberration and beam divergence had yet to be determined, as was the degree to which these instrumental effects would smear out detail. Also, in Fig. 7, images are shown as a function of thickness for the 435-reflexion two-dimensional multislice calculation. It can be seen that, for this structure, even for large changes in thickness, there is not much change in image profile. This coincides with experimental observations of images from wedge-shaped crystals.

In Fig. 8, Column 5, is shown the effect, on a series of calculated images, of summing images from scattering calculations for 11 angles of incidence across the cone of convergence. The summation consisted of addition of intensities, and not phases and amplitudes, since the source can be regarded as incoherent and, in this respect, is exactly similar to diffraction in a convergent-beam diffraction camera (Cockayne, Goodman, Mills & Moodie, 1967). As can be seen, the effect of divergence is zero at zero defect of focus and is increased as the absolute value of defect of focus increases. In fact, quite a good approximation to the divergence can be made by taking the beam image for one angle of incidence and shifting and adding image intensities. The amount of the shift is linearly dependent on the magnitude of the defect of focus.

Chromatic aberration arises from two sources, thermal spread of energy of emission in the source and energy loss in the specimen. This may be represented by adding images over a range of defects of focus about a mean value. The amount of this depth of focus is dependent on an individual microscope and its operating conditions. In this case, images were summed over ± 10 nm in 2 nm steps. In Fig. 8, Column 2, is shown the effect of this. Chromatic aberration due to energy loss in the specimen was not taken into account. The Figure shows that chromatic aberration has a very small effect on image profile.

In Fig. 8, Columns 3 and 4 show images calculated with spherical aberration coefficients of 3 and 5·1 mm respectively. It can be seen that this has a great effect on the calculated images. It was also found to be strongly dependent on aperture size and had less effect for smaller apertures.

All the above effects may be combined to give calculated images suitable for comparison with experiment (Fig. 8, Column 6). As is shown in Paper I, good agreement can be obtained with experiment if the full two-dimensional multislice calculations are used as input for image calculations.

In Fig. 9 is shown, for near focus, image calculations made from the full two-dimensional calculations for thin crystals compared with profiles of total projected charge density. These calculations were made for 11 beams for crystals ranging in thickness from 5 to 40 nm. It can be seen that for 10 nm crystals and range of defect of focus of ± 30 nm, the image intensity can be quite well represented by the product of defect of focus with projected charge density, and the calculated images show the reversal of contrast on passing through zero defect of focus. This simple approximation can be seen to break down for thicker crystals or larger defects of focus.

6. Conclusions

For very thin crystals, where the image contrast is seen to reverse on passing through zero defect of focus, then the simple projected charge density calculation is quite accurate for the limits of resolution of the ex-
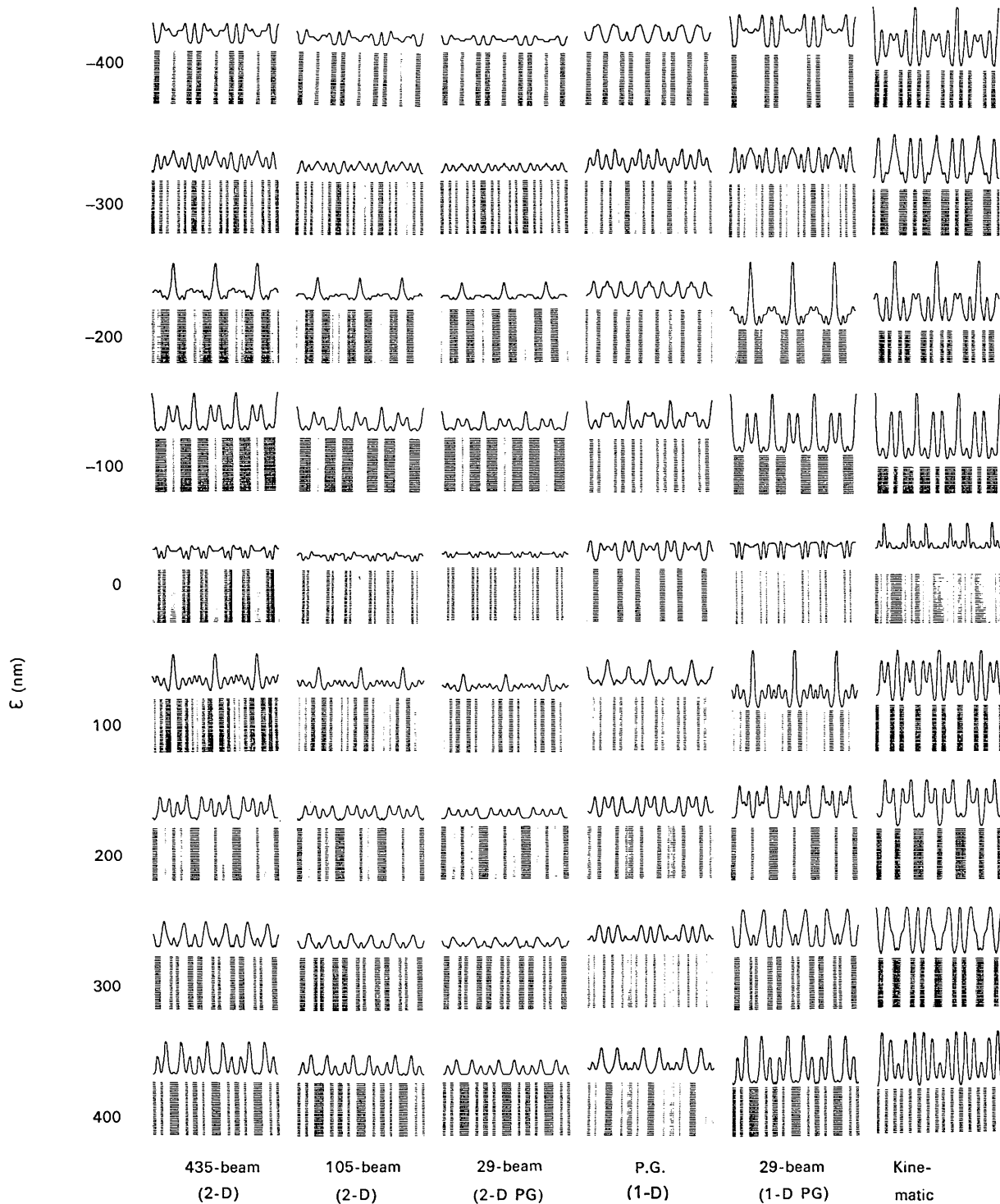
Fig. 6. Image contrast displayed both graphically and by half-tone display for crystal thickness of 30 nm for defects of focus ranging from −400 nm at the top of the display to +400 nm at the bottom in steps of 100 nm. The individual pictures are three unit cells wide. The images are calculated for eleven diffracted beams through the objective aperture. The vertical columns are in turn from left to right, 435 reflexion two-dimensional multislice calculation, 105 reflexion two-dimensional multislice calculation, systematics from a two-dimensional phase grating, one-dimensional phase grating, systematics from a one-dimensional phase grating, kinematic calculation.

periment. Near zero defect of focus, the contrast should be linearly dependent on magnitude of defect of focus. In other words, image features under these conditions can be naively interpreted as variation in charge density of the object. It must be emphasized that we are talking here of the total charge density of the material (electrons and nuclei) not just the electronic charge as is used in X-ray structure analysis. The range of crystal

Fig. 7. Image contrast for a range of defects of focus ranging from −400 nm at the top of the display to +400 nm at the bottom in steps of 100 nm. The columns are arranged for crystal thicknesses ranging from 10 nm to 60 nm in steps of 10 nm from left to right. The calculations are from the 435 reflexion two-dimensional multislice method. There is only a small variation in image contrast as a function of crystal thickness.
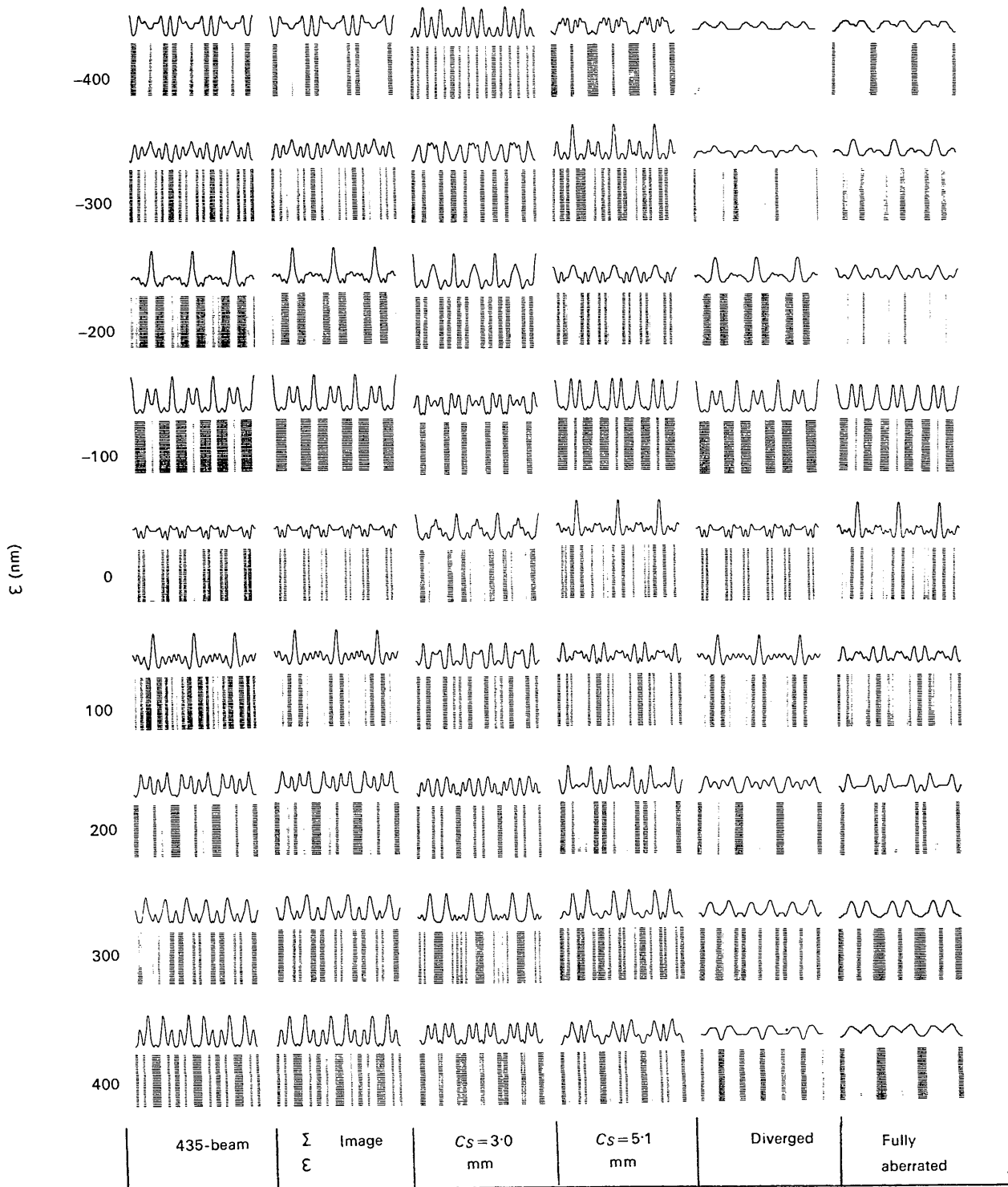
Fig. 8. Effect of aberrations on image contrast. The images are ranged from top to bottom as a function of defect of focus, −400 nm to +400 nm in steps of 100 nm. Column one is the unaberrated images as calculated using 11 reflexions from a 435 reflexion two-dimensional multislice calculation. Column two is the effect of chromatic aberration by summation of images over a depth of focus of 20 nm. Column three is the effect of incorporating a spherical aberration coefficient of 3·0 mm in the image. Column four is the effect of a spherical aberration coefficient of 5·1 mm. Column five is the effect of beam divergence of 1·3 × 10⁻³ radian. Column six is the effect of the combination of chromatic aberration, spherical aberration coefficient of 5·1 mm, and beam divergence of 1·3 × 10⁻³ rad.
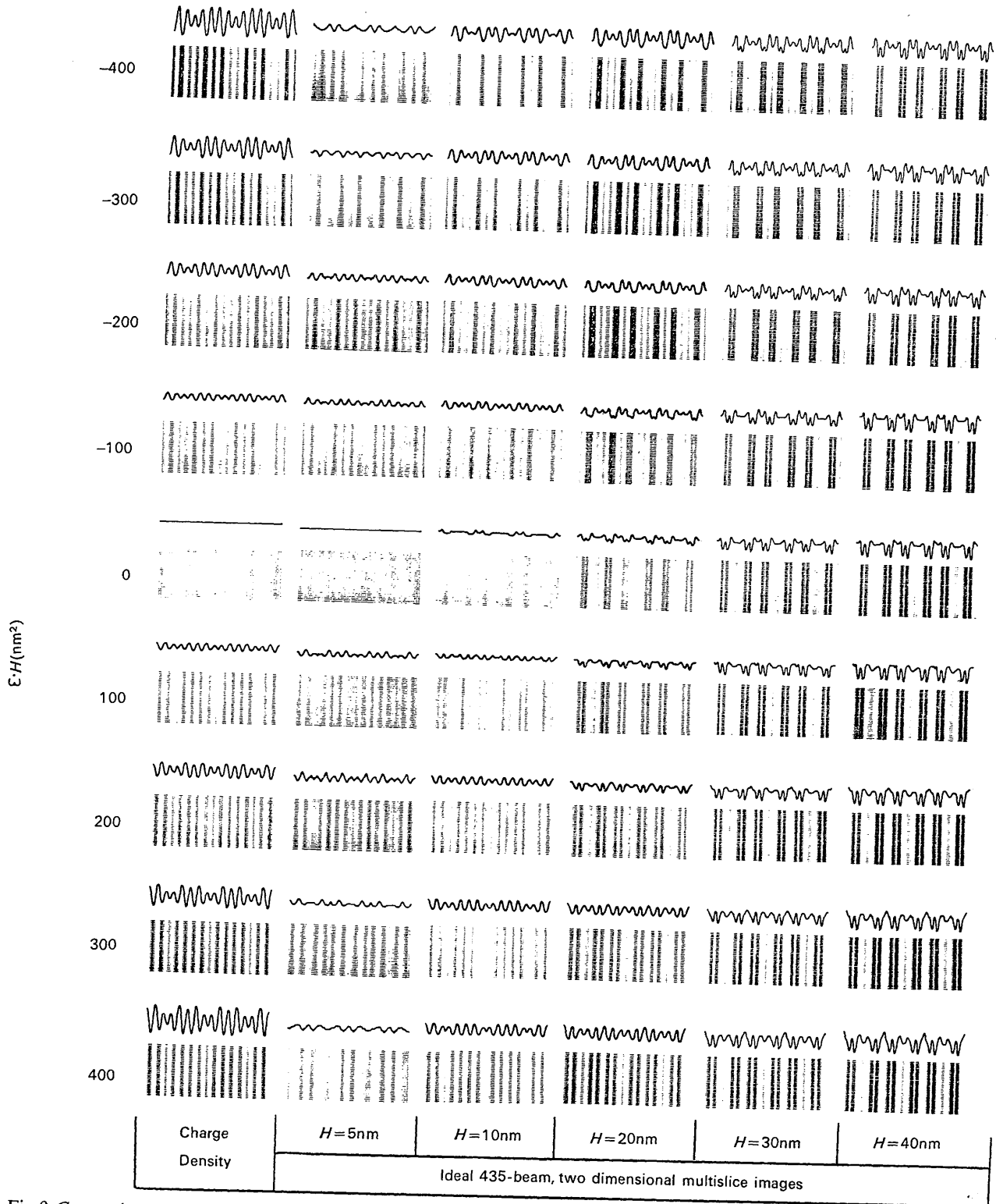
Fig. 9. Comparison of the charge density approximation with 435 reflexion, two-dimensional multislice calculation. The images are for 11 reflexions through the aperture. The charge-density calculation is column one on the left. Columns two to six are for crystal thicknesses 5, 10, 20, 30 and 40 nm. Zero defect of focus is 5 steps from the bottom. The ordinate of the display is chosen as the product defect of focus times crystal thickness since, in the charge-density approximation, image intensity is linearly dependent on both these quantities.

thicknesses for which this approximation will hold will be structure dependent, dependent on the microscope acceleration voltage and will become more accurate for higher voltages, although at higher voltages for the same contrast more defect of focus will be required.

The type of approximation in scattering theory to be used is also going to vary with the structure being examined. Although in this structure, and for comparatively thin crystals, large two-dimensional multislice calculations were used to obtain a good fit with experiment, this may not always be necessary. In fact, although the smaller two-dimensional multislice calculation and the systematic multislice calculation from a two-dimensional phase grating were quite poor with regard to calculation of diffracted beam intensity as a function of crystal thickness due to heavy weak-beam absorption, images calculated from both these methods are in reasonable agreement with experiment after the effects of the various aberrations are included. In similar structures even simpler methods may apply. In particular, calculations made on $TiNb_{24}O_{62}$ show that the systematics multislice from a one-dimensional phase grating is adequate.

The effect of instrument aberrations can be included in calculations in a systematic fashion and the principal effect is, as one might expect, that of averaging and blurring out of detail in the images.

The authors are grateful to Mr A. F. Moodie for helpful discussion about the methods of calculation used, and to Dr J.V. Sanders and Mr J. Allpress for the experimental information used, also to Mr G. R. Anstis for development of some of the programs.

One of us (M.A.O'K.) is grateful to the Division of Chemical Physics for permission to carry out this work there. Thanks are due to Mr E. Beckhouse for carrying out much tedious photography in the preparation of the figures.

References

ALLPRESS, J. G., HEWAT, E. A., MOODIE, A. F. & SANDERS, J. V. (1972). Acta Cryst. A28, 528.
ANDERSSON, S., MUMME, W. G. & WADSLEY, A. D. (1966). Acta Cryst. 21, 802.
ANSTIS, G. R., LYNCH, D. F., MOODIE, A. F. & O'KEEFE, M. A. (1972). Acta Cryst. To be published.
COCKAYNE, D. J. H., GOODMAN, P., MILLS, J. C. MOODIE, A. F. (1967). Rev. Sci. Instrum. 38, 1097.
COWLEY, J. M. & MOODIE, A. F. (1957). Acta Cryst. 10, 609.
COWLEY, J. M. & MOODIE, A. F. (1960). Proc. Phys. Soc. 76, 378.
CROMER, D. T. & WABER, J. T. (1965). Acta Cryst. 18, 104.
GOODMAN, P. & LEHMPFUHL, G. (1967). Acta Cryst. 22, 14.
GOODMAN, P. & MOODIE, A. F. (1972). Submitted to Acta Cryst.
HEAD, A. K. (1967). Aust. J. Phys. 20, 557.
HEWAT (née CHIDZEY), E. A. (1970). M. Sc. Thesis, Department of Physics, Univ. of Melbourne.
HOERNI, J. A. (1956). Phys. Rev. 102, 1534.
JOHNSON, A. W. S. (1968). Acta Cryst. A24, 534.
LYNCH, D. F. (1971). Acta Cryst. A27, 399.
MOTT, N. F. (1930). Proc. Roy. Soc. A127, 658.
ZERNIKE, F. (1942). Physica, 9, 686.

The Effect of Freezing on Precipitating Solids

BY O. FLINT

Chemical Engineering Division,
U.K.A.E.A. Research Group, Atomic Energy Research Establishment, Harwell, England

The major effect of a freeze/thaw treatment on aqueous gels, sludges or slurries is a decrease in crystallite size either by compressive or shear stresses, built up as a consequence of the increase in volume during the water to ice phase transformation. This change in crystallite size together with the freezing potential developed, leads to a reduction or neutralization in the positive particle charges, which results in accelerated precipitation on thawing.

Introduction

Settling, sedimentation or filtration of precipitating solids, particularly if gelatinous, is a tedious, time-consuming laboratory chore and in industry can be a major problem, particularly in the case of water treatment. Here the disposal of the by-product, (a sludge containing variable quantities of miscellaneous solids and water, according to the district and type of water treatment employed), can account for more than half the total treatment cost (Swanwick & Davidson, 1961). In addition valuable land must be used for settling lagoons, to limit bulk handling of drained material.

Any change in the handling of precipitating solids, therefore, leading to substantial savings in time or cost, would be of enormous benefit. Such a change was